THE ASTROPHYSICAL JOURNAL, 376:223–233, 1991 July 20

A POWERFUL LOCAL SHEAR INSTABILITY IN WEAKLY MAGNETIZED DISKS. II. NONLINEAR EVOLUTION

JOHN F. HAWLEY AND STEVEN A. BALBUS
Virginia Institute for Theoretical Astronomy, Department of Astronomy, University of Virginia, PO Box 3818, Charlottesville, VA 22903
Received November 1, 1990; accepted 1991 January 16

ABSTRACT

We consider the dynamical evolution of an accretion disk undergoing Keplerian shear flow in the presence of a weak magnetic field. A linear perturbation analysis presented in a companion paper shows that such a flow is dynamically unstable; here we consider some nonlinear consequences of this instability. We solve the equations of compressible magnetohydrodynamics using a two-dimensional finite-difference code. The Keplerian disk is threaded with a weak magnetic field that has a magnetic energy density much less than the thermal pressure. When perturbations are small, the numerical results are consistent with linear perturbation theory. We demonstrate the scaling relation between the instability's wavenumber and the Alfvén velocity that was found in the companion paper, and confirm that the maximum growth rate is independent of magnetic field strength. Neither compressibility nor the presence of toroidal field have a significant effect on the evolution of unstable modes. The most important dynamic effect is the redistribution of angular momentum leading to a strong interchange instability. The resulting radial motions produce field geometries that are conducive to reconnection, suggesting a possible mechanism for mode saturation. Even for very weak fields, whose most unstable wavelengths are small, nonlinear evolution results in the growth of structure on large scales. Total magnetic field energy increases by about one order of magnitude over the course of the simulations.

Subject headings: hydromagnetics — instabilities — stars: accretion

1. INTRODUCTION

In paper I (Balbus & Hawley 1991) we present a linear stability analysis for an accretion disk with magnetic field. We obtain the remarkable result that the presence of weak magnetic fields leads to a powerful local shearing instability. This result suggests that the full magnetohydrodynamic (MHD) equations must be solved when studying accretion disks, even for field strengths traditionally considered to be negligible. It has long been thought that a weak field will grow by shearing in an accretion disk, and that moderate strength fields can transfer angular momentum between fluid elements, possibly serving as a viscosity. It is clear that strong fields, with an energy density on order the thermal energy density, can significantly affect the disk, notably through magnetic buoyancy instabilities. However it now appears that field-disk interactions are dominated by a dynamical *instability* that inevitably results in exponentially growing magnetic fields and rapid angular momentum transfer. While idealized unmagnetized disks are extremely stable, astrophysical disks must be violently unstable, and the Rayleigh stability criterion is largely irrelevant. The existence of this instability is strong evidence for the oft-made assumption that accretion disks are turbulent.

In this paper we extend the linear analysis of paper I by carrying out numerical MHD simulations. Our goals are twofold. First, we wish to make the physical nature of the instability more palpable. Second, we seek some understanding of the nonlinear consequences of this instability through extended numerical stimulation. While there have been some recent MHD simulations of accretion disks, these have not explored the region of parameter space where this instability is operative. For example, the Parker instability has been studied by Matsumoto *et al.* (1990), but the initial magnetic energy density was on order of the thermal energy density, and—more significantly—angular momentum was neglected. Shibata & Uchida (1989) and Norman & Stone (1990) have simulated magnetically driven winds from disks, but in these studies the initial disk was not in equilibrium (it was sub-Keplerian), and was threaded with a strong magnetic field with an energy density in excess of the thermal energy density. Studies such as these have shown some dynamical effects of *strong* magnetic fields in accretion disks. However, as we have emphasized, *weak* magnetic fields are themselves of great importance and cannot be neglected.

In this work we concentrate on a simple section of a Keplerian disk threaded by a vertical magnetic field. The details of this model are described in § 2.1. The relation between the present work and the results of paper I is made explicit in § 2.2. The numerical techniques and diagnostics are outlined in § 2.3, and the results of the simulations are presented in § 3. These include a systematic investigation of the consequences of various initial field strengths, plus specific tests of other physical effects such as the effects of compressibility and a nonzero initial toroidal field. We present our conclusions in § 4.

2. PROBLEM CONFIGURATION AND NUMERICAL TECHNIQUE

2.1. *The Initial Model*

Since our aim in this paper is to provide a clear elucidation of the basic physics of the magnetic instability, we choose a particularly simple initial state. We consider a small region within a Keplerian flow in cylindrical coordinates, effectively reducing the accretion disk to a Keplerian cylindrical Couette flow. The grid is centered on R and extends in radius from $R - a$ to $R + a$ with a vertical thickness of a. We assume purely radial gravitational and centrifugal forces; there are no vertical pressure or density gradients. The assumption of

Keplerian flow means that gravitational and centrifugal forces are initially in radial balance. The angular velocity Ω is the Keplerian value at R. Pressure and density are taken to be constant throughout the box. Most, but not all of the simulations use an ideal gas equation of state with $\gamma = 5/3$. For simplicity, we use periodic boundary conditions on z and reflecting boundary conditions on the radial walls of the box.

These initial conditions are an acceptable representation of an accretion disk so long as the numerical grid is a small region centered about the disk's midplane. Self-consistency requires the grid scale a to be much less than R, the radial distance from the central gravitating mass, and H, the vertical scale-height of the disk at R. For comparison, an isothermal Keplerian disk has a vertical scale-height that is related to the sound speed c and the angular velocity Ω by

$$H^2 \sim 2c^2/\Omega^2 . \tag{2.1}$$

The physics of this ideal MHD simulation is scale-free. In the absence of forces in the z direction, the physically important length and time scales are set by Ω, the periodicity length in the z direction, here chosen to be equal to a, and the poloidal Alfvén speed v_A. The essential parameters are the ratios c/Ω and v_A/Ω. For convenience we set $GM = 1$ and center the grid at $R = 100$; this makes the Keplerian angular velocity at that point equal to 10^{-3}. Again for convenience we take $\rho = 1$, and choose the gas pressure $P = 10^{-5}$. Thus the ratio of the isothermal sound speed to the angular velocity at R is 10, giving a scale-height $H \sim 14$. For the simulation domain we choose a vertical thickness of $a = 1$ so that the simulation grid can be regarded self-consistently as a small region centered around R with a periodicity length in z that is a fraction of H.

We investigate the evolution of the magnetic instability by placing weak magnetic fields onto this hydrodynamically stable initial model. For most of the simulations we begin with a uniform z-field of finite radial extent, placed in the center of the grid. The magnetic field is set by choosing β_z, the ratio of gas to poloidal magnetic pressure,

$$\beta_z = \frac{P}{(B_z^2/8\pi)} . \tag{2.2}$$

When desired, we add a uniform toroidal field, similarly parameterized by β_ϕ. We have examined several initial field configurations.

2.2. *Connection with Linear Theory*

In paper I we show that the instability does not depend directly on the field strength, but only on the product of the poloidal Alfvén speed v_A over the angular velocity times the physical wavenumber. It is useful to define a normalized vector wavenumber parameter q that makes this explicit, writing

$$q_i = k_i v_A/\Omega , \tag{2.3}$$

where i can be either R or z.

In the numerical simulations we do not know *a priori* which wavevector $\boldsymbol{k}$ will emerge. The unstable modes that develop will be influenced by the grid size, the boundary conditions, and the initial field and perturbation. As a guideline, however, we can compute growth rates and wavelengths for a variety of wavenumbers scaled in terms of the periodicity length of the grid. Since we are considering the idealized case of a Keplerian distribution of angular velocity in a constant density and pressure background, the linear perturbation results of paper I can be written in a very simple form. The growth rate obtained from linear theory, after setting the Brunt-Väisälä frequency to zero, is found to be (eq. [2.9] of paper I)

$$\frac{\omega^2}{\Omega^2} = q_z^2\left\{1 - \frac{8}{[\kappa^2/\Omega^2 + (\kappa^4/\Omega^4 + 16\, q^2)^{1/2}]}\right\} , \tag{2.4}$$

where $q^2 = q_z^2 + q_R^2$, and the term κ is the epicyclic frequency; for a Keplerian disk $\kappa/\Omega = 1$. From equation (2.4) we see that the shortest unstable wavelength has $q^2 = 3$. By setting this critical wavelength equal to the periodicity length in the numerical grid, $\lambda_{\rm crit} = a = 1$, we find that $\beta_z = 266$ corresponds to the maximum field strength for which the instability should be present. The mode with wavenumbers $q_z = 1$, $q_R = 0$ has the maximum linear growth rate ($=0.75\Omega$); this corresponds to $\beta_z = 800$ for a wavelength of a. Note that because we have artificially imposed a small scale height a, the instability is stabilized at much weaker field strengths than it would be in a completely self-consistent disk. For example, in a Keplerian disk with scale height H, the instability will be present so long as the minimum unstable wavelength is less than the disk thickness, a condition which is satisfied for $\beta_z \gtrsim 1$.

2.3 *Numerical Technique*

We solve the standard equations of compressible ideal MHD (paper I, eq. [2.1]) in cylindrical coordinates through the use of finite-difference techniques. We assume infinite conductivity (flux-freezing). The numerical techniques for the hydrodynamics are essentially the same as those employed in earlier simulations of disk instabilities (Hawley 1990), except that we substitute cylindrical coordinates for the pseudo-Cartesian coordinates used in that earlier study. The basic approach is time-explicit, staggered-mesh, operator-split finite-differencing (e.g., Norman & Winkler 1986). Field evolution is handled within the framework of the constrained transport method (Evans & Hawley 1988). The constrained electromotive forces in the induction equation and the transverse $\boldsymbol{J} \times \boldsymbol{B}$ forces are constructed using information obtained along upwind Alfvén characteristics. The numerical techniques will be described in another paper (Norman et al. 1991). These MHD techniques have undergone extensive testing on a wide variety of problems (Stone et al. 1991).

The numerical mesh is divided into equally spaced zones in R of width ΔR, and equally spaced zones in z of width Δz. Several grid resolutions have been used ranging from the lowest resolution grid of 64×64 zones to the finer meshed (R, z) grid of 256 by 128 zones. We use the low resolution grid to carry out a survey of various field configurations and strengths while computing selected models at higher resolution.

One of the key diagnostics used in these simulations is a measure of the power in various Fourier components obtained by integrating over the periodic interval in z

$$f(R) = \int_0^a B_R(R, z) e^{ik_z z/a}\, dz , \tag{2.5}$$

and then averaging over radius the log of the norm of this complex-valued function

$$\frac{1}{(R_{\rm out} - R_{\rm in})} \int_{R_{\rm out}}^{R_{\rm in}} \ln|f|\, dr . \tag{2.6}$$

TABLE 1

z-FIELD SIMULATIONS: RANDOM PERTURBATION

Model	(R, z) Grid	β_z	Orbits	$\tilde{k}_z = 1$	$\tilde{k}_z = 2$	$\tilde{k}_z = 3$	$\tilde{k}_z = 4$	$\tilde{k}_z = 5$	$\tilde{k}_z = 6$
1a	64 × 64	100	2.2	...	...	...	...	...	...
1b	64 × 64	100	2.9	0.69	0.36	...	...	...	...
2a	64 × 64	1000	3.0	0.70	0.23	...	...	...	...
2b	256 × 128	1000	3.3	0.61	0.20	...	...	...	...
3a	64 × 64	4000	2.7	0.37	0.67	0.63	0.32	...	...
3b	256 × 128	4000	3.5	0.42	0.65	0.59	0.26	...	...
4a	64 × 64	16000	2.8	0.26	0.40	0.55	0.59	0.51	0.57
4b	256 × 128	16000	3.7	0.20	0.44	0.53	0.63	0.61	0.60

The radial average is carried out over the middle quarter of the grid. One can then obtain growth rates for various wavenumbers by means of a least-squares fit during the linear growth period for comparison with the linear perturbation theory of paper I. As a second diagnostic we monitor the total poloidal and toroidal magnetic energy densities on the grid as a function of time. These are obtained by direct integration over the entire domain.

As a numerical test we have run an unmagnetized, purely hydrodynamical simulation using this grid. We perturbed the initial disk by altering the angular momentum in a small region of circular cross section. As expected, the resulting ring executed characteristic epicyclic motion. Not a trace of instability was seen. But, as we show below, a very small magnetic field makes for a much different story.

3. SIMULATIONS

3.1. *Instabilities of Weak z-Fields*

We begin with a series of simulations designed to demonstrate most clearly the essential physics of the instability. Consider a pure z-field placed in a narrow region in the center of the grid, from $R - a/5$ to $R + a/5$. The intention in confining the field to a narrow radial band is to isolate the resulting dynamic evolution, and minimize the effect of the reflecting radial boundaries. As it turns out, this choice of initial field configuration has its own set of nonnegligible consequences, but these too can be isolated and understood.

We perturb the initial conditions by varying the specific enthalpy by a small, random amount (between $\pm$ 1%) in every grid zone. The resulting pressure perturbations create small random velocities. This means that all the wavenumbers available to the grid (i.e., from $2\pi/a$ down to $\pi/\Delta z$) are excited at very low amplitudes. Table 1 lists the results from a series of simulations with random initial perturbations, providing the model number, the grid resolution, the length of time to which the simulation was run, and the growth rate of the averaged Fourier component of the radial magnetic field in units of Ω for the first six z wavenumbers (eq. [2.6]).

Model 1a is a relatively strong z-field simulation with $\beta_z = 100$. The minimum unstable wavelength for this field is $\lambda_{\min} = 1.62$, larger than the periodicity length $a = 1$. Thus, there exist no unstable z wavelengths on this grid for this field strength. This model was run for 2.2 orbits. Figure 1*a* is a plot of time-dependence of the k_z ($\equiv \tilde{k}_z/2\pi$) = 1 and $\tilde{k}_z = 6$ Fourier components of the radial magnetic field. The plot shows no growth, as expected.

As a control we increase the grid size by setting $a = 3$ while retaining the same initial field of $\beta_z = 100$. The larger physical extent of the grid is the only difference between Model 1b and

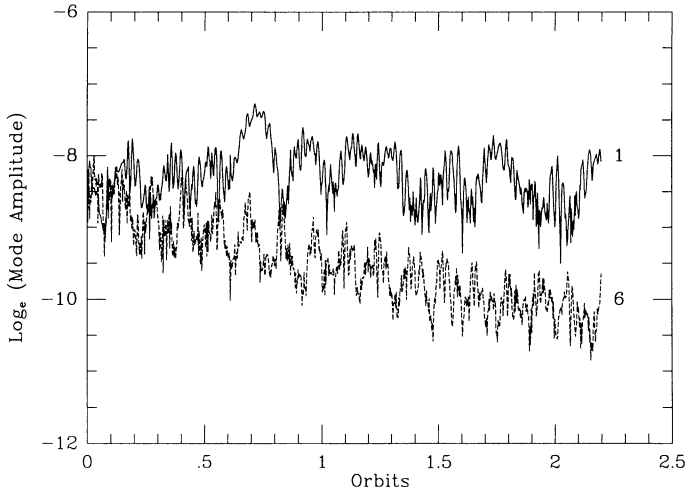

FIG. 1*a*

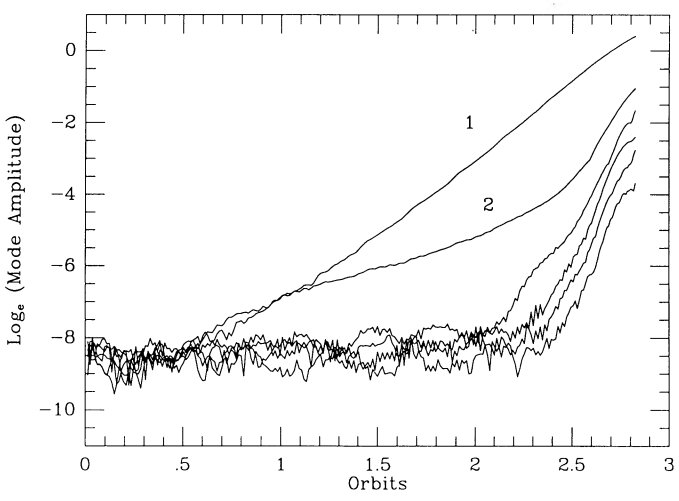

FIG. 1*b*

FIG. 1.—(*a*) Time-dependence of the $\tilde{k}_z \equiv k_z/2\pi = 1$ and $\tilde{k}_z = 6$ Fourier components of the radial magnetic field in the $\beta_z = 100$, $a = 1$ simulation (Model 1a). This model shows no mode growth. (*b*) Time-dependence of $\tilde{k}_z$ wavenumbers 1 through 6 for the $\beta_z = 100$, $a = 3$ simulation (Model 1b). Increasing the periodicity-length of the grid over that of Model 1a allows unstable modes. Wavenumbers 1 and 2 show linear growth; higher wavenumbers are linearly stable. Growth due to nonlinear mode coupling begins at 2.2 orbits.

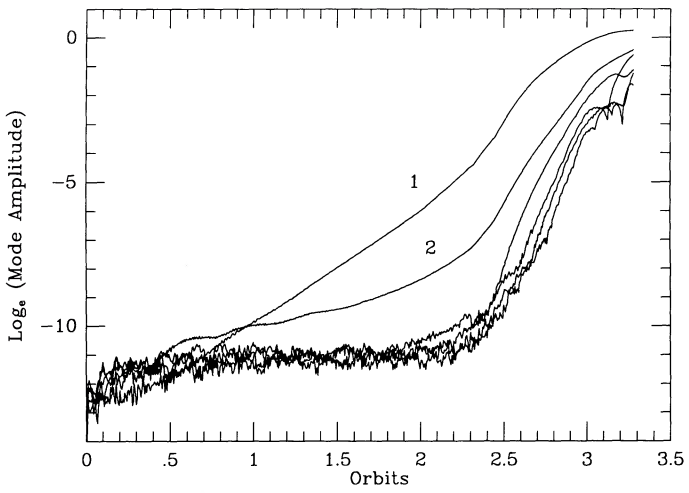

FIG. 2.—Time-dependence of $\bar{k}_z$ wavenumbers 1 through 6 for the $\beta_z = 1000$, $a = 1$ high-resolution simulation (Model 2b). As in Model 1b, only $\bar{k}_z = 1$ and 2 are unstable. However, the periodicity-length of the grid is the smaller value corresponding to that used in Model 1a. In Model 2b, the instability is enabled by decreasing the magnetic field strength.

Model 1a. In Model 1b, both the $\bar{k}_z = 1$ and $\bar{k}_z = 2$ Fourier components are growing; higher wavenumbers are not (see Fig. 1*b*). The growth rates are given in Table 1. Two things are apparent from the comparison with linear theory. First, the $\bar{k}_z = 1$ growth rate is slightly smaller than the value obtained from linear theory for a $q_z = 1$, $q_R = 0$ mode of wavelength $a = 3$. Because we have a rather restricted radial grid, it is not possible to have modes with $q_R = 0$, so it is not surprising that the growth rate should be less than the maximum pure z value. Second, a pure $\bar{k}_z = 2$ mode should be stable according to the linear analysis of paper I. As discussed in § 3.2 below, the observed growth in the $\bar{k}_z = 2$ mode is due to the choice for initial magnetic field configuration.

In Model 2 the amplitude of the magnetic field is decreased to $\beta_z = 1000$. For this field strength the minium unstable wavelength is 0.513. Figure 2 is the plot showing B_R Fourier mode amplitudes as a function of time for the high-resolution run (model 2b). The growth rate for the $\bar{k}_z = 1$ mode is 0.61. The $\bar{k}_z = 2$ mode has a growth rate of 0.19 for the first two orbits and then a growth rate of 1.26 after. This latter growth rate, equal to twice that of the $\bar{k}_z = 1$ mode, represents nonlinear mode coupling. Distinct nonlinear effects become apparent after six $\bar{k}_z = 1$ e-folding times. All the higher wavenumbers are linearly stable, although they too grow from nonlinear coupling after only 2.5 orbits.

Figure 3 consists of plots of the poloidal magnetic field lines, angular momentum, and toroidal field at the end of the simulation. It is immediately apparent that the presence of a weak magnetic field leads to a classic interchange instability. There are two regions where the angular momentum has been significantly modified. The upper blob has had its angular momentum reduced and it is moving inward (to the left) while the lower blob has had its angular momentum increased, resulting in an outward motion. Where the poloidal magnetic field has been stretched out radially, a toroidal field is generated. For these model parameters, the instability continues to grow until the field lines encounter the radial grid boundaries.

The total poloidal field energy is obtained by integrating over the numerical grid. At the beginning of the simulation this is equal to 4×10^{-9}. (Note that initially the total thermal energy $E_{\text{thermal}} = 2 \times 10^{-5}$, and the field energy is smaller than β_z times this value because the field initially occupies only a portion of the grid.) The poloidal field energy increases by a factor of 5 (to 2×10^{-8}) between orbits 2.8 and 3.3. Field energy generation proceeds during the linear growth phase through amplification of the *perturbed* field, and this becomes significant compared to the initial field energy only after large-scale motions in the fluid begin. For this model, the energy in the toroidal field is initially zero. The initial perturbations generate a small B_ϕ component giving a total energy density $\sim 10^{-15}$ after one orbit. In the remaining 2.3 orbits of the simulation the total toroidal field energy grows to 2×10^{-8}. Thus, although the field strength has grown due to the instability, its total energy remains well below the thermal energy. Nevertheless, dramatic readjustment in the structure of the disk is occurring due to the transfer of angular momentum between fluid elements.

The next two models are designed to investigate the effects of decreasing the strength of the magnetic field while holding the grid scales constant. As the magnetic field weakens the most unstable wavelengths decrease proportionally. For example, by increasing β_z to 4000 (Model 3) we reduce the minimum unstable wavelength by a factor of 2, $\lambda_{\text{min}} = 0.25$, and the fastest growing wavelength is reduced to 0.45. Model 4 with $\beta_z = 16000$ decreases these wavelengths by a further factor of 2.

Figure 4 shows the Fourier amplitudes as a function of time for Model 3b, the high-resolution, $\beta_z = 4000$ simulation. The fastest growing wavenumbers are $\bar{k}_z = 2$ and 3; $\bar{k}_z = 5$ and 6 are stable. The evolution becomes nonlinear at orbit 2, after which all modes grow at a very rapid rate. The longest wavelength model, $\bar{k}_z = 1$, is unstable with a growth rate of 0.42Ω, reduced from the value in Model 3. Nonlinear mode coupling comes into play after two orbits, after which the growth rate in the $\bar{k}_z = 1$ mode increases to 1.32Ω.

In Figure 5 we plot the poloidal field lines, the toroidal field, and the angular momentum at orbit 3.3. As with Model 2, the instability produces regions of high and low angular momentum that are moving radially through the grid. As they do so, the poloidal field lines are stretched out. A further consequence can be seen in Figure 5; X-points form in the field. Although there is no explicit finite conductivity in the numerical code, the field can numerically reconnect when there is oppositely directed field within one grid zone. This is occurring here. The resulting field loops surround regions of reduced (or increased) angular momentum. The minimum and maximum values of angular momentum present on the grid at this time correspond to Kepler orbits at $R = 97$ and 103; recall that the grids runs from $R = 99$ to 101.

Figure 6 shows the averaged Fourier amplitudes as a function of time for Model 4b, the high-resolution, $\beta_z = 16{,}000$ simulation. The slowest growing wavenumber is $\bar{k}_z = 1$; the higher wavenumbers listed in Table 1 are all unstable with rapid growth rates. After two orbits, the long wavelength $\bar{k}_z = 1$ mode grows much more rapidly due to nonlinear coupling. This is a point worth reemphasizing: although the wavelength of the most rapidly growing mode decreases with field strength, the long wavelengths remain unstable, albeit with lower growth rates. Furthermore, as seen in this simulation, nonlinear effects transfer power from short to long wavelengths as well as from long to short. Hence, even very weak fields, whose most unstable wavelengths are quite small, can create large-scale effects in the disk.

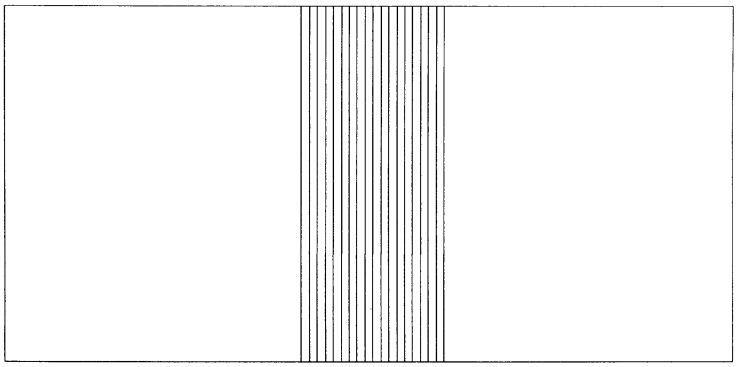

FIG. 3*a*

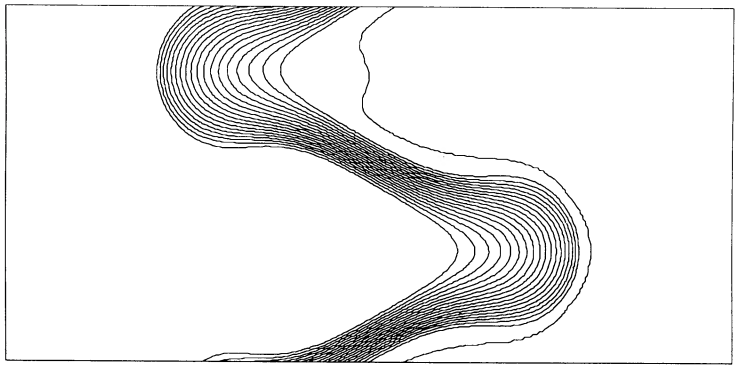

FIG. 3*b*

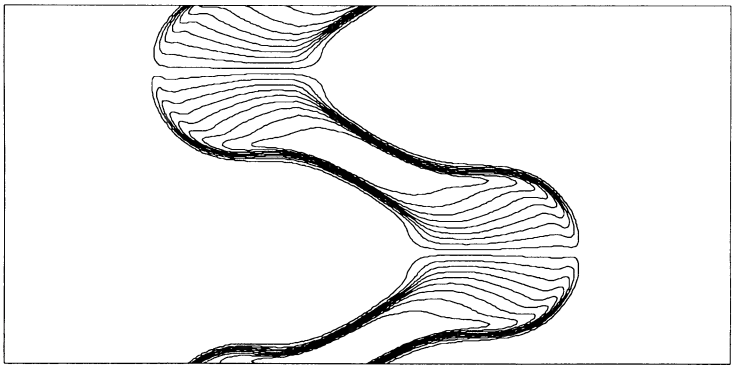

FIG. 3*c*

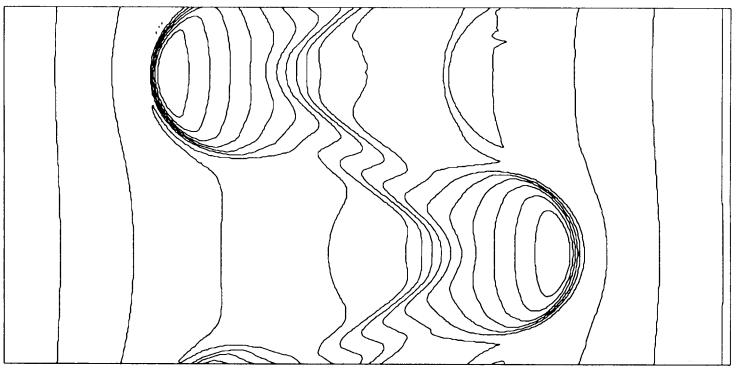

FIG. 3*d*

FIG. 3.—Contour plots of (*a*) the *initial* poloidal magnetic field lines, and (*b*) the poloidal magnetic field lines, (*c*) toroidal field, and (*d*) angular momentum at 3.3 orbits in the $\beta_z = 1000$, $a = 1$ high-resolution simulation (Model 2b). There are 20 linearly spaced contours. The angular momentum values run from 9.91 to 10.08; the Keplerian value of the angular momentum at the center of the grid is 10. The toroidal field has a maximum energy density of 2×10^{-7}.

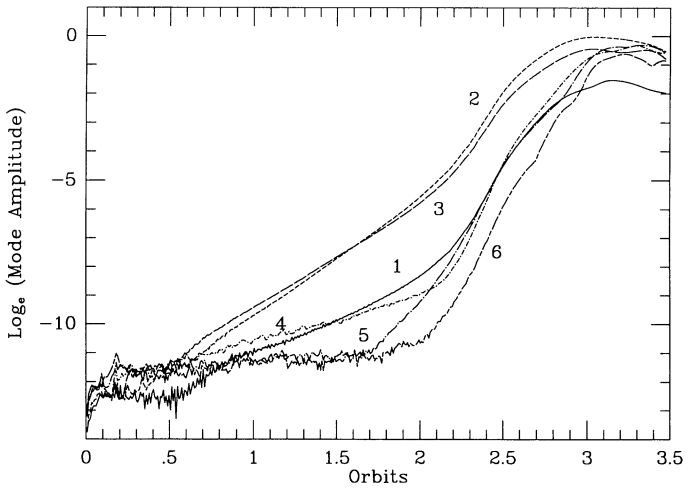

FIG. 4.—Time-dependence of $\bar{k}_z$ wavenumbers 1 through 6 for the $\beta_z = 4000$, $a = 1$ high-resolution simulation (Model 3b). The curves are labeled by their wavenumbers. Decreasing the field strength by a factor of 2 has made wavenumber 1 through 4 unstable; $\bar{k}_z = 5$ and 6 stable. Each curve is labeled by number.

Figure 7 shows the results of the instability at 3.2 orbits. The fastest growing pure z wavelength would be 0.222. On the simulation grid that wavelength is closest to $\bar{k}_z = 4$, and this is reflected in the number of large spikes and bubbles that have formed. The fastest growing wavelengths dominate through the course of the linear evolution and into the nonlinear phase. The angular momentum in the bubbles has a minimum value of 9.913, corresponding to a Kepler orbit $R_{\rm Kep} = 98$, and a maximum of 10.09 corresponding to $R_{\rm Kep} = 102$. Note that these extreme specific angular momentum values are functions only of the mode growth time, not of the strength of the magnetic field. The size of the bubbles depends on the wavelength of the unstable mode, but the specific angular momentum within that bubble, and hence the radius of its new Keplerian orbit, does not. The exchange of angular momentum between fluid elements will continue until some nonlinear effect ends it. One such effect is reconnection. As the simulations demonstrate, the radial fluid motions quickly lead to field configurations that favor such reconnection.

The random perturbations create an initial toroidal field with a total energy density of 3×10^{-16}. By the end of the simulation this has grown to 6×10^{-9}. The poloidal field begins with total energy 3×10^{-10} and peaks at 1.4×10^{-8} by orbit 3.2. The field energy then drops because of (numerical) field reconnection. The bubbles become isolated field loops and the field that defined the spikes leading to the bubbles becomes a length of (mostly) z-field near the center of the grid. At this location the angular velocity has become nearly constant with radius. Such a local angular velocity distribution can be sustained only because the grid's radial reflecting boundaries permit compensating pressure gradients.

Together, Models, 2, 3, and 4 provide a numerical demonstration of the scaling relation between mode growth and the parameter q: the growth rates of the unstable modes are independent of the field strength alone, depending only on the product of wavenumber and Alfvén speed over angular velocity. The data in Table 1 are summarized in Figure 8 where we plot growth rates as a function of q_z. Also plotted are the linear growth rate curves corresponding to several radial wavenumbers. The spread in values at a given wavenumber q_z provides an estimate of the numerical error-bars associated with both the simulation and the procedure used to obtain a growth rate. It is clear that the radial wavenumbers are not zero. In fact the modes represented here are radial averages, and must contain power from several modes of various permissible radial wavenumbers. The anomalous growth at $q_z = 1.78$ is discussed in the next section.

3.2. *The Critical Wavelength*

One obvious inconsistency between the linear stability results and the numerical simulations listed in Table 1 and plotted in Figure 8, is the observed growth for the wavenumber $q_z = 1.78$. This wavenumber is greater than the critical wavenumber $q_{\rm crit} = \sqrt{3}$, but in both Models 2 and 4 this mode is clearly unstable, albeit with a slow growth rate. In this section we describe experiments that investigate this phenomenon.

The first question to ask is, could this be a numerical effect? After all, in Model 2a the difference between the critical wavelength and the wavelength of the $\bar{k}_z = 2$ mode, $\lambda = 0.5$, is less than Δz, and the higher resolution simulations in both Model 2 and Model 3 have lower growth rates than the low resolution case. However, there is no good indication that this mode growth is simply numerical, given the range of resolutions and wavelengths tested. As one additional test of the "numerical" hypothesis we compute a 64×64 grid model with $\beta_z = 250$. For this magnetic field strength, the wavelength in question corresponds to the periodicity length of the grid, i.e., $\bar{k}_z = 1$. The results indicate that the mode grows with a rate 0.30Ω.

We consider next a physical, rather than numerical, cause. From paper I we know that the instability is due to the inability of stabilizing magnetic tension to overcome the destabilizing centrifugal force in a displacement. Any additional forces can either be stabilizing or destabilizing. In the set of simulations listed in Table 1 we consider an isolated region of magnetic field at the center of the grid. This means there will be a small magnetic pressure force directed outward from this region. The hypothesis is that this pressure acts as an additional destabilizing force and accounts for the observed growth. To test this idea, we use a new set of initial conditions with a uniform z-field throughout the grid. This will eliminate the magnetic pressure gradients due to the initial poloidal field. We run simulations on the 64×64 grid for $\beta_z = 250$, 1000, 4000, and 16000. We apply the same initial random enthalpy perturbation as were used in the simulations of Table 1. The resulting growth rates are listed in Table 2. For these simulations, no linear mode growth occurs for the $q_z = 1.78$ wavelengths. This result is consistent with our hypothesis; the additional background magnetic pressure gradient, present because of our initial conditions, acts to destabilize wavelengths near the critical value. The comparison between these two sets of simulations provides a satisfying demonstration of the balance of forces that is responsible for the critical wavelength.

3.3 *Effect of Compressibility*

The linear perturbation analysis of paper I was derived using the Boussinesq approximation, appropriate to an analysis of noncompressive waves. However, since the numerical code solves the fully compressible MHD equations, it is possible to investigate the effects of compressibility on the instability. To do this we repeat Model 2a for two different equations of state, $\gamma = 2$ and $\gamma = 4/3$. For all three equation-of-state gammas, the

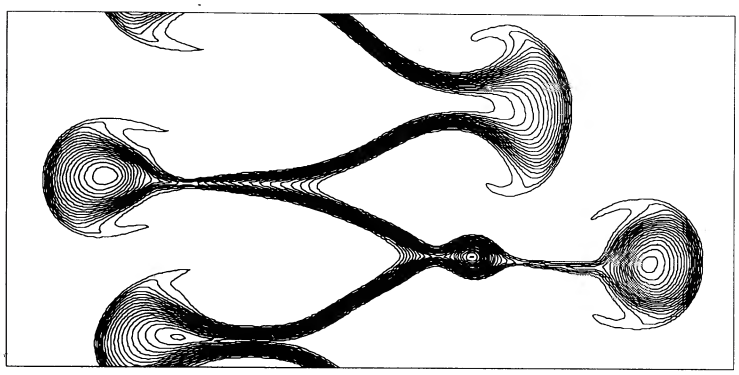

FIG. 5a

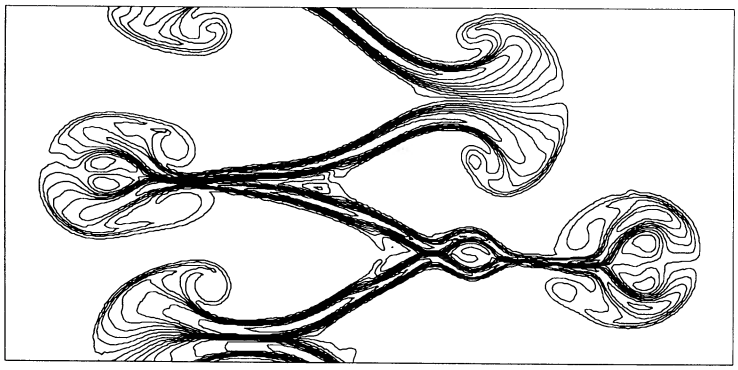

FIG. 5b

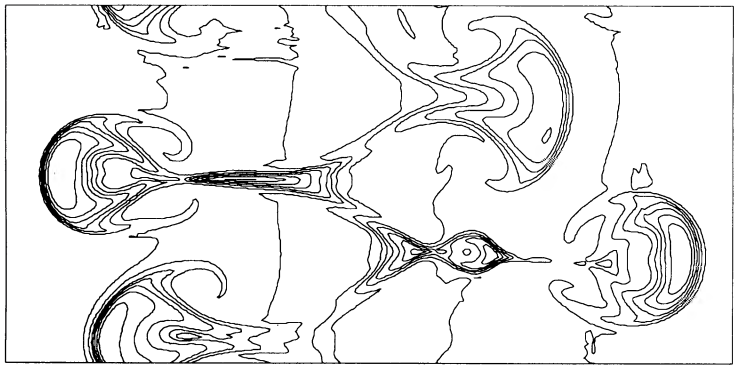

FIG. 5c

FIG. 5.—Contour plots of (*a*) the poloidal magnetic field lines, (*b*) toroidal field, and (*c*) angular momentum at 3.3 orbits in the $\beta_z = 4000$, $a = 1$ high-resolution simulation (Model 3b). There are 20 linearly spaced contours. The angular momentum values run from 9.86 to 10.14; the Keplerian value of the angular momentum at the center of the grid is 10. The toroidal field has a maximum energy density of 2×10^{-7}. At this time the z-length scale of the most prominent structures has been determined primarily by the wavelength of the fastest growing mode, $k_z = 2$.

evolution of the instability is essentially the same, as are the derived growth rates for the unstable modes. We conclude that, as anticipated, the instability is not altered by compressibility, nor by the choice of equation of state, although, as demonstrated by the experiments of § 3.2, pressure forces can play a role in determining the critical wavelength for the onset of the instability.

3.4 *Effect of Toroidal Field*

So far, all the numerical models have assumed zero initial toroidal field. The linear analysis shows that the instability and its growth rates are independent of toroidal field strength if the Boussinesq approximation holds. This will be the case so long as the toroidal field energy density is less than the thermal energy density, $\beta_\phi > 1$. As a check, we do a simulation using the parameters of Model 2a, and add a relatively strong, constant toroidal field with $\beta_\phi = 10$. (A toroidal field that is much stronger would be interesting in its own right, as it would be prone to buoyancy instabilities in a vertically stratified accretion disk.) The instability proceeds as before with the same growth rates. The main difference is that the random perturbations work with the strong toroidal field to produce larger

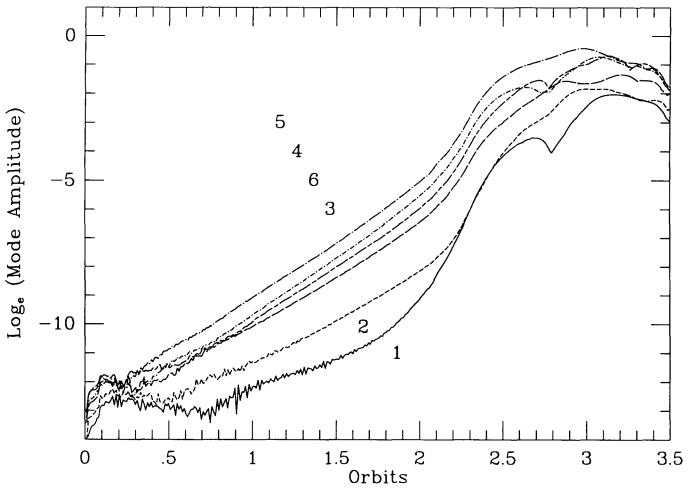

FIG. 6.—Time-dependence of k_z wavenumbers 1 through 6 for the $\beta_z = 16000$, $a = 1$ high-resolution simulation (Model 4b). All wavenumbers 1 through 6 are now unstable. The individual curves are indicated by number.

initial poloidal field perturbations. These larger initial perturbations mean that instability reaches nonlinear saturation sooner than in the otherwise equivalent Model 2a. We conclude that the instability can operate effectively even in the presence of relatively strong toroidal fields such as those expected in an accretion disk.

3.5. *Instabilities in Field Loops*

We have considered the evolution of the magnetic instability for initial configurations involving both toroidal and z-fields. Another general field topology to consider is the poloidal field loop. We observed in the earlier simulations that field loops are a likely consequence of the nonlinear evolution of a z-field. Further, one expects that field loops would be present *ab initio* in an accretion disk. We are therefore led to consider a vector potential of the form

$$A_\phi = \frac{\beta}{2} \ln\left[\frac{1}{(R - R_c)^2 + (z - z_c)^2 + 1}\right], \qquad (3.1)$$

for all $[(R - R_c)^2 + (z - z_c)^2] < r_{\rm lim}^2$, and constant otherwise, to produce circular field lines centered on (R_c, z_c) out to the limiting radius, $r_{\rm lim}$. The parameters β, $r_{\rm lim}$, and the constant in the denominator can be adjusted as desired. Here we choose $\beta = 1000$, and $r_{\rm lim} = 1/12$, and center the field loops on the 256×128 grid used in the high resolution simulations of Table 1.

Figure 9 shows the time evolution of the field. The initial configuration was randomly perturbed, as before. The final frame pictured in Figure 9 for this simulation is at 2.0 orbits. After one orbit the field loop begins to stretch out radially. Fluid elements have exchanged enough angular momentum to bring the loop out of equilibrium with it surroundings. Between 1 and 2 orbits the total poloidal field energy increases by a factor of 10 from its initial value of 10^{-10}. The toroidal field energy is zero initially, although the presence of a radial field assures linear toroidal field growth regardless of the efficacy of the instability. By two orbits the toroidal field energy has grown to 3×10^{-8}. At two orbits the minimum and maximum angular momentum values in the "mushroom caps" are 9.94 and 10.06. This simulation demonstrates that loops of poloidal field are capable of efficiently transferring angular momentum and driving the instability. The radial stretching of field loop appears to lead to a field configuration that is conducive to true dissipative reconnection.

4. CONCLUSIONS

Before summarizing our conclusions, we reiterate the various experiments done as controls and tests of the numerics. Simulations performed without magnetic fields show that the disk is hydrodynamically stable; rings that are perturbed by altering their specific angular momentum merely execute epicyclic motion. We have examined both strong and weak field configurations, and the same field strength on two grids with different periodicity lengths. This procedure tests the scaling relation between field strength and wavenumber. During that portion of the simulations for which the perturbations are small, the results are consistent with the linear perturbation theory of paper I. As discussed in § 3.2, when a uniform field is used as an initial condition (as opposed to an isolated z-field) we observe no growth for wavelengths shorter than the critical value obtained from the linear analysis. Both low- and high-resolution simulations yield the same qualitative results. In addition we have been able to test some of the limits of the linear theory. In particular we confirm that neither compressibility nor toroidal field have a significant effect on the instability.

These simulations begin to explore new territory when the unstable mode amplitudes become large. Strong mode-mode coupling can be seen in the plots of mode amplitude versus time. Both longer and shorter wavelengths can feed off power in the fastest growing mode. Although the most unstable wavelengths for very weak fields are quite small, larger wavelengths are still unstable, and the nonlinear evolution assures the growth of structure on large scales.

The most important dynamic effect is the redistribution of angular momentum. In the simulations we find that significant angular momentum is transferred between fluid elements connected by the magnetic field. This occurs on the length scales of the unstable modes. This transfer results in a strong inter-

TABLE 2

UNIFORM z-FIELD SIMULATIONS

(R, z) Grid	β_z	$k_z = 1$	$k_z = 2$	$k_z = 3$	$k_z = 4$	$k_z = 5$	$k_z = 6$
64×64.....	250	...	...	...	...	...	...
64×64.....	1000	0.63	...	...	...	...	...
64×64.....	4000	0.47	0.68	0.63	...	...	...
64×64.....	16000	0.32	0.51	0.55	0.64	0.66	0.54

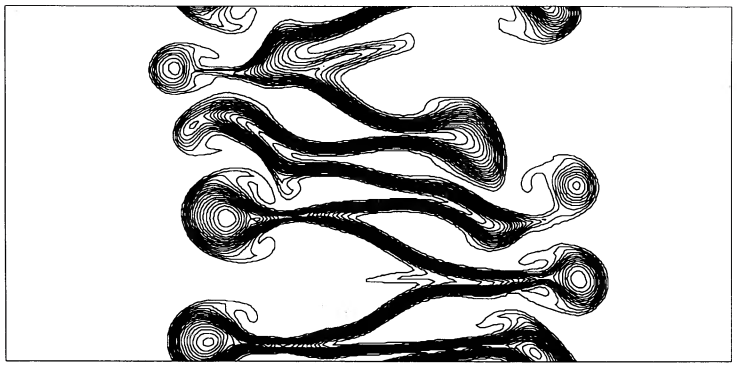

FIG. 7*a*

FIG. 7*b*

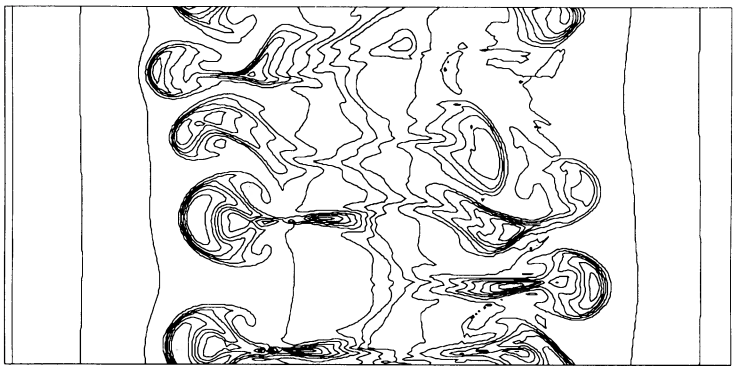

FIG. 7*c*

FIG. 7.—Contour plots of (*a*) the poloidal magnetic field lines, (*b*) toroidal field, and (*c*) angular momentum at 3.2 orbits in the $\beta_z = 16000$, $a = 1$ high-resolution simulation (Model 4b). There are 20 linearly spaced contours. The angular momentum values run from 9.91 to 10.09. The toroidal field has a maximum energy density of 2×10^{-7}.

change instability as bubbles of low or high angular momentum form and find themeselves far out of equilibrium with the surrounding gas. In all cases the angular momentum in a bubble corresponds to a Kepler orbit at a radius whose distance from the initial equilibrium location greatly exceeds the linear wavelength of the instability. Comparing simulations using field loops with those using pure z-fields indicate that the ability to transfer angular momentum is not strongly dependent on field topology. In addition, we observe that total magnetic field energy increases over the initial value by about one order of magnitude during the nonlinear growth.

How does the mode finally saturate, and how will it operate in an actual accretion disk? Because of the limited nature of the simulations presented here we can only offer suggestions. As discussed in paper I, there seem to be two possibilities: (1) the field may grow until the minimum unstable wavelength exceeds the thickness of the disk, or (2) reconnection may limit the field amplitude, leading to dissipative turbulence. The present simulations clearly favor the second possibility. The instability operates so vigorously to redistribute angular

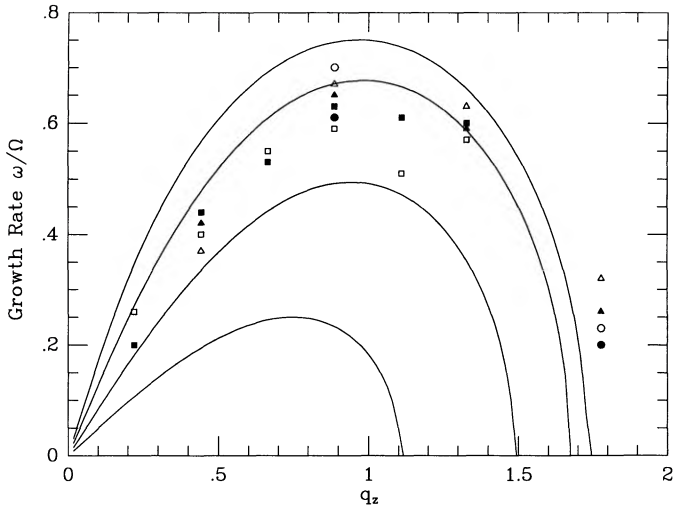

FIG. 8.—Growth rates as a function of q_z for simulations listed in Table 1. Curves represent values obtained from linear theory for $q_R = 0., 0.44, 0.89$, and 1.33. The squares correspond to Model 4, the triangles to Model 3, and the circles to Model 2. Filled symbols represent the high-resolution simulations, open symbols represent the low.

momentum that the disk is far from equilibrium long before the initial field strength is greatly increased. Furthermore, the large radial excursions in the fluid that result from the redistribution of angular momentum, stretch out the field, providing the opportunity for field reconnection to occur. The resulting loops of poloidal field can themselves drive the instability.

Accepting that any arguments must necessarily be crude, if we adopt the turbulence picture, what is the functional dependence of the resulting viscosity? The length scale at which reconnection occurs should be roughly proportional to the most unstable wavelength, $\sim v_A/\Omega$, while typical mixing velocities should be of order this length times Ω. This suggests that

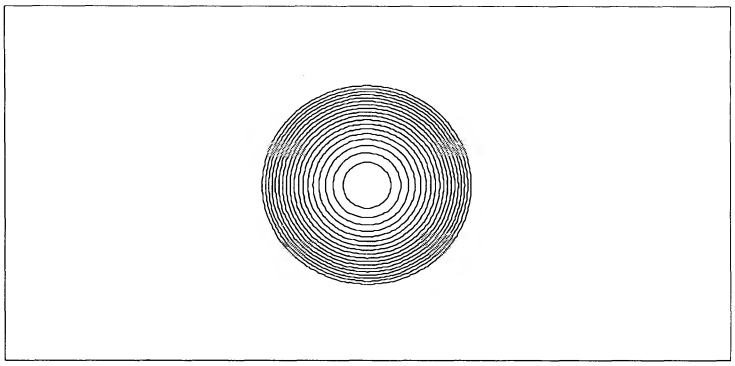

FIG. 9*a*

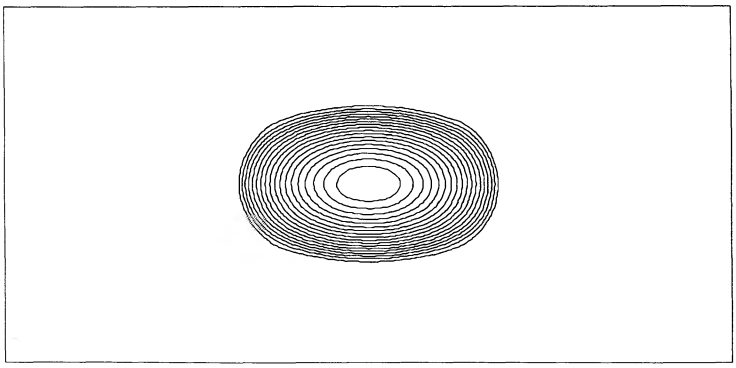

FIG. 9*b*

FIG. 9.—Poloidal magnetic field lines at (*a*) 0.4 orbits, (*b*) 0.8 orbits, (*c*) 1.2 orbits, (*d*) 1.6 orbits, and (*e*) 2.0 orbits for the evolution of a poloidal field loop. The extreme values of angular momentum in the mushroom caps at 2.0 orbits are 9.94 and 10.06, corresponding to Kepler orbits at $R = 99$ and 101.

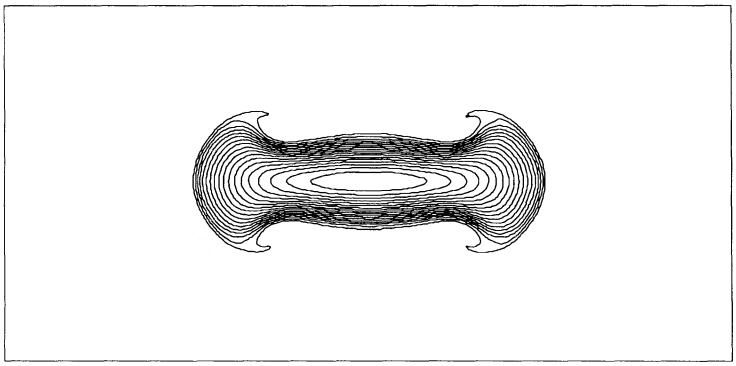

FIG. 9c

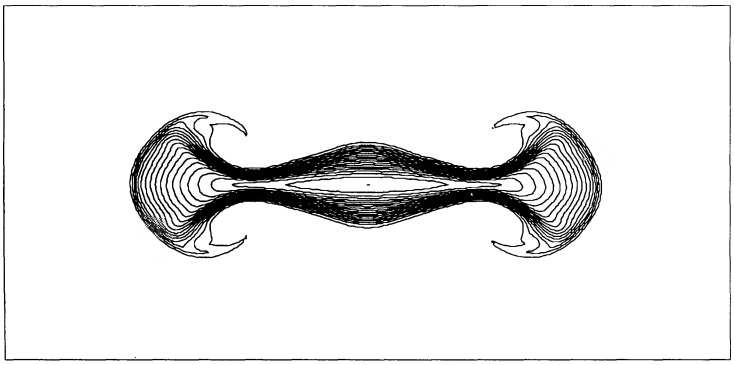

FIG. 9d

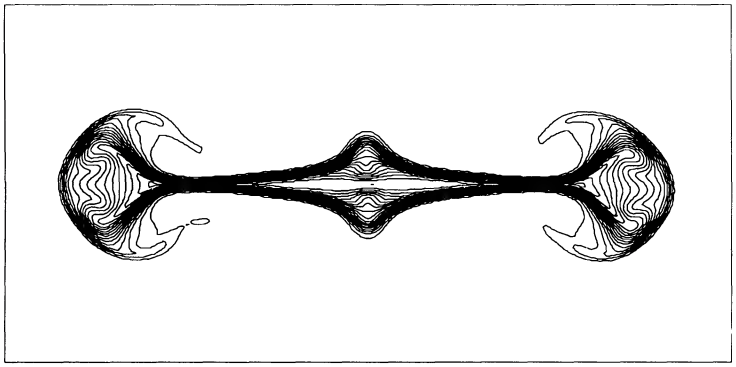

FIG. 9e

the viscosity should be $\nu \sim v_A^2/\Omega$, i.e., viscosity is a function of magnetic pressure. At this point, however, we lack a self-consistent picture of what the average magnetic field strength in a turbulent disk will be.

In both this paper and in paper I, we have shown that an initially turbulence-free Keplerian disk is dynamically unstable in the presence of a weak magnetic field. We feel that this is a very promising source of turbulence in accretion disks. In future work we will address the role of the instability in more complex initial disk models, as well as the important question of nonaxisymmetric instabilities.

This work is partially supported by NSF grants PHY-8802747 and AST-8820293, and NASA grants NAGW-1510 and NAGW-764. Computations were carried out on the Cray XMP system of the National Center for Supercomputing Applications, and the Cray YMP at the NASA Center for Computational Science.

REFERENCES

Balbus, S. A., & Hawley, J. F. 1991, ApJ, 376, 214 (I)
Evans, C. R., & Hawley, J. F. 1988, ApJ, 332, 659
Hawley, J. F., 1990, ApJ, 356, 580
Matsumoto, R., Horiuchi, T., Hanawa, T., & Shibata, K. 1990, ApJ, 356, 259
Norman, M. L., & Stone, J. M. 1990, in Galactic and Extragalactic Magnetic Fields, ed. R. Beck, P. Kronberg, & R. Wielebinski (Dordrecht: Reidel), in press
Norman, M. L., Stone, J. M., Evans, C. R., & Hawley, J. F. 1991, in preparation
Norman, M. L., & Winkler, K-H. 1986, in Astrophysical Radiation Hydrodynamics, ed. K-H. A. Winkler & M. L. Norman (Dordrecht: Reidel), p. 187
Shibata, K., & Uchida, Y. 1989, in Theory of Accretion Disks, ed. F. Meyer, et al. (Dordrecht: Kluwer), p. 65
Stone, J. M., Hawley, J. F., Norman, M. L., & Evans, C. R. 1991, in preparation